Check for updates

Breaking the axiality of pentagonal−bipyramidal dysprosium(III) single-molecule magnets with pyrazolate ligands†

Zi-Han Li, Yuan-Qi Zhai, Wei-Peng Chen, Qian-Cheng Luo, Tian Han (iD) and Yan-Zhen Zheng (iD) *

A range of pyrazolate-based ligands have been used to balance the multidentate-chelating feature and the magnetic axiality in "destroyed" pentagonal-bipyramidal (DPB) dysprosium(III) single-molecule magnets (SMMs). This family of complexes are air-stable and share the general formulae of $[DyX^1X^2(L_{eq})_5][BPh_4]$, where X^1 and X^2 are the anionic axial ligands, including pyrazolate-based ligands and chloride; L_{eq} is the equatorial solvent molecule such as tetrahydrofuran (THF), pyridine (py) and thiazole (NS). Compared to the prototype PB SMMs, the bidentate-chelating features of the pyrazolate ligands show, albeit slow magnetic relaxation behavior, a much smaller energy barrier for magnetization reversal (U_{eff}). Static electronic calculation shows that the magnetic axiality above the ground $m_J = \pm 15/2$ states has been much reduced, leading to the mixing of other states at higher levels. Nevertheless, this systematic study reveals that the variation of the substituents on the pyrazolate ligands and the replacement of planar solvents are effective at influencing the magnetic relaxation behavior. We found that the chloride coordinating mono-pyrazolate complexes, such as $[DyX^1Cl(THF)_5][BPh_4]$ (X^1 = 3-(trifluoromethyl)pyrazole (tfpz) **1**, X^1 = 3-methylpyrazole (Mepz) **2**, X^1 = 3-isopropyl-1*H*-pyrazole (Iprpz) **3**, X^1 = 3,5-dimethyl-pyrazole (Me$_2$pz) **4**, X^1 = 3,5-diisopropylpyrazole (Ipr$_2$pz) **5**, and X^1 = pyrazole (pz) **6**, generally show lower U_{eff}, while bi-pyrazolate complexes, such as $[Dy(tfpz)_2(THF)_5][BPh_4]$ **7**, $[Dy(pz)_2(THF)_5][BPh_4]$ **8**, $[Dy(pz)_2(py)_5][BPh_4]\cdot 2py$ **9** and $[Dy(pz)_2(NS)_5][BPh_4]$ **10**, show higher U_{eff}. Among them, **8** shows the largest U_{eff} of 521(8) K and a comparable open hysteresis temperature of ∼5 K (at a field sweeping rate of 12 Oe s^{-1}) with **9** and **10**. The enhanced blocking temperature for **8** is different from that for the PB Dy(III) SMMs in which the py ligand can cause a much higher hysteresis temperature than the one coordinated with THF due to the aromatic π−π interactions, indicating that the bis-bidentate-chelating Dy(III) ion is rigid enough to reduce the influence from the equatorial ligands. Moreover, substitution with electron-withdrawing groups such as the ⁻CF$_3$ group reduces U_{eff} prominently. Such a clear magnetostructural correlation in Dy(III) SMMs is fundamentally important, indicating that a subtle balance between magnetic axiality and molecular rigidity is critical to design high-performance Dy(III) SMMs.

Introduction

The development of high-temperature single-molecule magnets (SMMs) requires not only a high energy barrier (U_{eff}) for magnetization reversal,[1–7] but also high stiffness to reduce the Raman process.[8] This is the essence behind the successful story of dysprosocenium-type SMMs, which progressively enhances the blocking temperature (T_B) to above the liquid nitrogen temperature (77 K).[9] The dysprosium(III) ion has been recognised as one of the most excellent candidates for high-performance SMM design because of the very large magnetization moment arising from the oblate electrostatic potential of the $^6H_{15/2}$ state.[10–14] This also implies that the ligands play an important role in enhancing the magnetic anisotropy of the Dy^{3+} ion.[15–19] Other than the inherent electrostatic property vibrations around the magnetic centre also affect significantly the dynamics of the magnetic moment. In particular, the Raman process which is compactly associated with molecular vibrations contributes to the fast magnetic relaxations.[20–22] Hence, the reduction of molecular flexibility is also critical.

Frontier Institute of Science and Technology (FIST), Xi'an Jiaotong University Shenzhen Research School, State Key Laboratory of Mechanical Behaviour for Materials, MOE Key Laboratory for Nonequilibrium Synthesis of Condensed Matter, Xi'an Key Laboratory of Sustainable Energy and Materials Chemistry, Xi'an Jiaotong University, 99 Yanxiang Road, Xi'an, Shaanxi 710054, P. R. China. E-mail: zheng.yanzhen@xjtu.edu.cn
†Electronic supplementary information (ESI) available: The structural figures and additional magnetic data of **1–10**. CCDC 1991398–1991407. For ESI and crystallographic data in CIF or other electronic format see DOI: 10.1039/d0qi00906g

This journal is © the Partner Organisations 2020

Inorg. Chem. Front., 2020, **7**, 4367–4376 | **4367**

Research Article

Inorganic Chemistry Frontiers

The use of η-cyclopentadienyl (Cp) and its derivatives successfully possesses these two virtues.[23–27] The Cp-based ligands provide six π electrons with a penta-dentate-chelating feature to strengthen the molecular rigidity. Hence, the Cp-based Dy(III) SMMs show much higher T_B though their U_{eff} is just comparable to that of another family of high barrier SMMs – the pentagonal-bipyramidal (PB) family of Dy(III) SMMs.[28–32] The latter suffers the uni-coordinating point on the axial position of the PB geometry, which is not firm enough to reduce the vibration caused Raman process. Though a recent strategy by using the intra/inter molecular π–π stacking interaction proves to be successful,[8] it is interesting to know whether using chelating ligands on the axial position of the PB geometry is effective at reducing the molecular vibration while maintaining the magnetic axiality.

This needs to be balanced. As we can see when the carbon rings are larger than five, such as η-arene (η^6-C_6R_6),[33] η-cycloheptatrienyl (η^7-C_7R_7),[34] η-cyclooctatetraenyl (η^8-C_8R_8)[35–41] and η-cyclononanetraenyl (η^9-C_9R_9),[41] the magnetic axiality is not retained like the cyclopentadienyl does. From an electrostatic standpoint, it could be argued that aromatic organometallic ligands with binding sites larger than η^5 cannot effectively stabilize the oblate electronic surface of the $M_J = \pm15/2$ state of the Dy(III) ion. Larger aromatic rings are more favorable for an electronic surface with prolate features, such as Er(III).[15] For this consideration we would not use larger-size chelating ligands.

The pyrazole ring is one of the easiest and most flexible N-donor heterocycles to incorporate into polydentate ligand structures. Its deprotonated pyrazolido ion ([pz]$^-$) can bind up to metal ions "end-on" through its N1 and N2 in η^2 mode, which may keep the balance between molecular vibration and magnetic axiality. Here we first try the bidentate pyrazole-based ligands to replace the mono-dentate alkoxide/phenoxide ligands in the PB system. The resulting ten complexes share the general formulae of $[DyX^1X^2(L_{eq})_5][BPh_4]$, where X^1 and X^2 are the anionic axial ligands, including pyrazolate-based ligands and chloride; L_{eq} is the equatorial solvent molecule such as tetrahydrofuran (THF), pyridine (py) and thiazole (NS). We found that the chloride coordinating mono-pyrazolate complexes, such as $[DyX^1Cl(THF)_5][BPh_4]$ (X^1 = 3-(trifluoromethyl)pyrazole (tfpz) **1**, X^1 = 3-methylpyrazole (Mepz) **2**, X^1 = 3-isopropyl-1H-pyrazole (Iprpz) **3**, X^1 = 3,5-dimethylpyrazole (Me$_2$pz) **4**, X^1 = 3,5-diisopropylpyrazole (Ipr$_2$pz) **5**, and X^1 = pyrazole (pz) **6**, generally show lower U_{eff}, while bi-pyrazolate complexes, such as $[Dy(tfpz)_2(THF)_5][BPh_4]$ **7**, $[Dy(pz)_2(THF)_5][BPh_4]$ **8**, $[Dy(pz)_2(py)_5][BPh_4]\cdot2py$ **9** and $[Dy(pz)_2(NS)_5][BPh_4]$ **10**, show higher U_{eff}. Compared to the prototype PB SMMs, this family of complexes shows much smaller U_{eff}, which we believe is due to the broken D_{5h} symmetry and hence, reduced magnetic axiality, which is confirmed by the *ab initio* calculations. Except for the obvious electron-withdrawing effect on the axial pyrazolate ligands, the equatorial solvent molecules have much less influence on the magnetic properties of this series of complexes, indicating the success of a strong bi-dentate-chelating effect from the pyrazolate ligands.
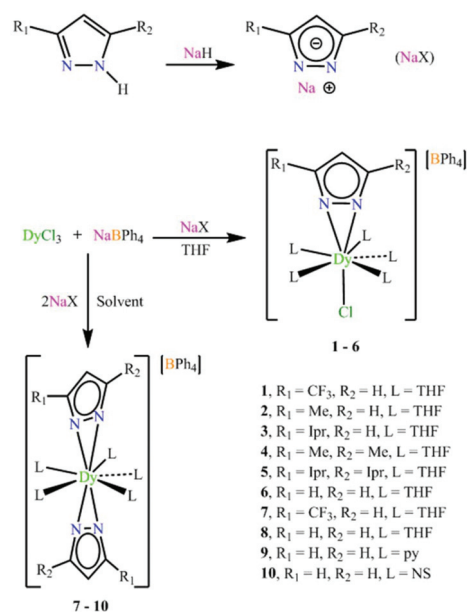
Results and discussion

Syntheses and structures

These ten complexes were prepared by two routes (Scheme 1). Complexes **1–6** were prepared by the reaction of DyCl$_3$ in THF with one equivalent sodium salt of pyrazolate ligands and NaBPh$_4$. Complexes **7–10** were prepared by an analogous procedure of **1–6** except for adding two equivalents of the sodium salt of pyrazolate ligands (see the ESI† for details). The final products are stable under ambient conditions.

The structures were analysed by single crystal X-ray diffraction (Fig. 1e–j). Complexes **1–6** comprise a mononuclear cation $[DyXCl(THF)_5]^+$, a charge-balancing anion BPh$_4^-$, one disordered THF and water molecules (for **4–6**). The coordination geometry about dysprosium can be envisioned as "destroyed" pentagonal-bipyramid (DPB) with five THF donor oxygen atoms in the equatorial plane, one N–N bond and one chloride in the axial positions. If the centroids of the nitrogen–nitrogen bonds of the η^2-pyrazolate ligands are considered, the DPB structure is formed.[42,43] The five equatorial Dy–O bond lengths range from 2.382(3) to 2.493(6) Å, which are a little longer than the axial Dy–cen(N–N) bonds (2.303(5) Å for **1**, 2.235(5) Å for **2**, 2.232(3) Å for **3**, 2.233(5) Å for **4**, 2.238(5) Å for **5** and 2.242(5) Å for **6**. The Dy–Cl bond lengths fall in the range of 2.608(1)–2.623(2) Å and the Cl–Dy–cen(N–N) angle ranges from 175.80(2)° to 177.94(6)° for **1–6**, displaying an essentially linear coordination of the negatively charged donor atoms. The nearest-neighbour equatorial O(THF)–Dy–O(THF) angles lie between 70.31(13)° and 73.44(13)°, highlighting the pseudo-

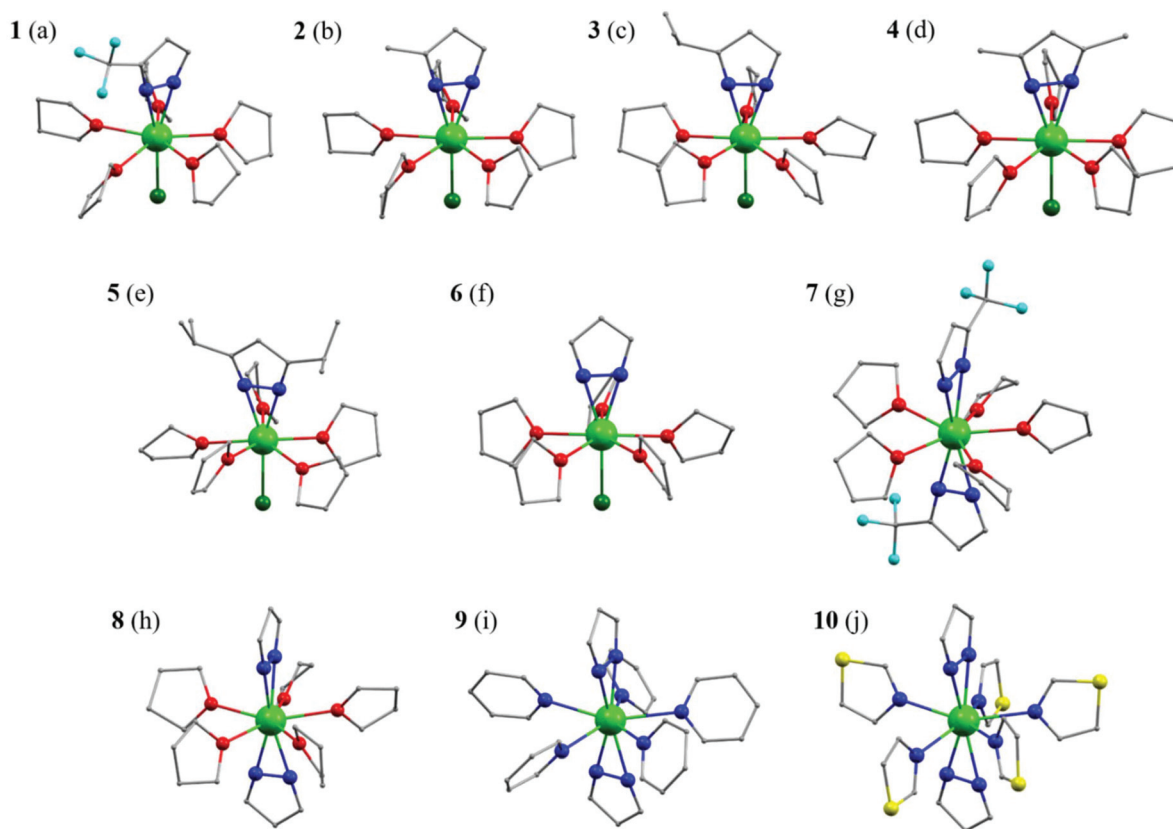**Scheme 1** Synthetic route for complexes **1–10**.

Fig. 1 Crystal structures of the $[DyX^1X^2(L_{eq})_5]^+$ cations in complexes **1–10** (labelled as a to j, respectively). Solvent molecules and hydrogen atoms are omitted for clarity. Colour codes: Dy, bright green; N, blue; O, red; F, turquoise; Cl, green; C, grey; S, yellow.

C_{5v} symmetry. Due to the large size of the tetraphenylborate anion, the metal centre is well isolated with the closest intermolecular metal⋯metal separations ranging from 8.009 to 8.328 Å (Fig. S3–S8†). The selected bond distances and angles for **1–6** are listed in Tables S1–S6.†

The central Dy(III) ions in complexes **7–10** are formally nine-coordinate with two pyrazolate ligands bound by their nitrogen atoms in η^2-fashion in the axial position instead. For **7**, the trifluoromethyl pyrazolate ligands are used and the average Dy–cen(N–N) is 2.306(5) Å and Dy–O(THF) bond lengths range from 2.421(3) to 2.531(3) Å. The cen(N–N)–Dy–cen(N–N) angle is almost linear (178.71(9)°), while adjacent O(THF)–Dy–O(THF) angles lie between 72.23(3)° and 73.06(7)°. These values are very close to the ideal angle (72°) for pentagonal bipyramidal geometry. When trifluoromethyl pyrazole is replaced by pyrazole, complex **8** is formed, which has a shorter average Dy–cen(N–N) of 2.283(8) Å. The cen(N–N)–Dy–cen(N–N) angle is 174.23(27)° and the O(THF)–Dy–O(THF) angles lie between 70.7(2)° and 75.5(2)°, giving a DPB geometry (Fig. 2). When planar THF molecules are substituted by pyridine and thiazole, complexes **9** and **10** are formed, respectively. The axial average Dy–cen(N–N) is 2.289(6) Å for **9** and 2.300(1) Å for **10**. The cen(N–N)–Dy–cen(N–N) angle is 177.66(22)° for **9** and 175.16(37)° for **10**, while N(pyridine)–Dy–N(pyridine) angles lie between 69.77(10)° and 76.52(10)° and N(thiazole)–Dy–N
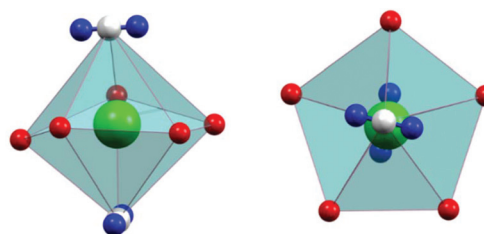

Fig. 2 The side and top view of the DPB polyhedron of **8**. Colour codes: Dy, bright green; N, blue; O, red; centroid of N–N, white.

(thiazole) angles lie between 69.58(14)° and 78.29(14)°, respectively. The shortest Dy⋯Dy separation for complexes **7–10** is similar, ranging from 9.947(7) Å to 11.466(3) Å (Fig. S9–S12†). The selected bond distances and angles for complexes **7–10** are listed in Tables S7–S10.†

Magnetic characterization

The temperature dependence of magnetic susceptibilities under 1000 Oe dc field was analysed. At room temperature, for all compounds, the $\chi_M T$ products (in emu K mol^{-1}) are in good agreement with the expected value of 14.17 emu K mol^{-1} for free Dy(III) ions ($S = 5/2$, $L = 5$, $g = 4/3$). Upon cooling, the $\chi_M T$

This journal is © the Partner Organisations 2020

Inorg. Chem. Front., 2020, **7**, 4367–4376 | **4369**

curve decreases steadily below 150 K before rapidly decreasing below 30 K for all ten complexes, which reflects thermal depopulation of the m_J sub-levels (Fig. S13 and S14†). The field-dependent magnetizations reach values in the range of 5.20–5.60μ_B per Dy(III) ion for all complexes at 2 K. The unsaturation values indicate the presence of anisotropy in all complexes. Low temperature magnetization studies also show a distinction between complexes **1–6** and **7–10**. Complexes **1–6** show a simple increase in $M(H)$, while **7–10** show S-shaped curves at 2 K suggesting a frozen effect (Fig. S15 and S16†).

Alternating current (ac) susceptibilities were measured in the frequency range of 1–1218 Hz (Fig. 3 and S17–S35†). Under zero dc field, only very small tail of out-of-phase (χ'') ac susceptibility signals could be observed above 2 K for **1**, which is possibly caused by a strong QTM effect, while other complexes show obvious frequency/temperature dependent in-phase (χ') and out-of-phase ac susceptibility signals. At a frequency of 1218 Hz, the maximum signal occurs between 16 K and 34 K for complexes **2–10**, where the maximal temperature (34 K) is found for **8**, suggesting that **8** may possess the highest barrier.

Cole–Cole plots were constructed from these data and fitted to the Debye model (Fig. S36–S48†).[44] The relaxation times τ were plotted *versus* T^{-1}. For complexes **2–5** and **7–10**, the plots are nearly-linear at high temperatures, slow curvature at intermediate temperatures and show temperature-independence at the lowest temperatures. A model including three possible relaxation processes (QTM, Raman and Orbach mechanisms) was employed to analyze the relaxation.

$$\tau^{-1} = \tau_{\text{QTM}}^{-1} + CT^n + \tau_0^{-1}\exp(-U_{\text{eff}}/T) \quad (1)$$

In this equation, C and n are parameters of the Raman process and τ_{QTM} is the rate of the quantum tunneling of magnetization (QTM). In the higher temperature regime, the Orbach relaxation process is dominant, acting as a thermally activated regime, while the Raman process makes a major contribution at intermediate temperatures and the QTM process appears when the temperature is below 10 K.

The curves were all fitted with eqn (1) and the key magnetic fit parameters are given in Table 1. We found that it is possible to fit the data of complex **1** using only the Raman process by the equation

$$\tau^{-1} = CT^n. \quad (2)$$

The best Raman fit gives $C = 0.045(2)$ s^{-1} K^{-n} and $n = 5.55$ (3). While

$$\tau^{-1} = CT^n + \tau_0^{-1}\exp(-U_{\text{eff}}/T) \quad (3)$$

with Orbach and Raman processes used for **6**, giving $C = 0.011(2)$ and $n = 2.83(4)$. Among the complexes with a halide on the pseudo five-fold axis of the DPB (complexes **1–6**), complex **6** possesses the highest U_{eff} value of 470(5) K. Complexes **7–10** have U_{eff} values between 380(5) and 521(8) K. The barrier for **8** appears largest at 521(8) K among all ten complexes.

To confirm the magnetization blocking, zero-field cooled and field cooled (ZFC–FC) magnetic susceptibility measurements were carried out with 2000 Oe dc field. The ZFC–FC plots show a divergence at about 4.5 K for **8–10** (Fig. 4a, S49 and S50†). The magnetic hysteresis shows butterfly shapes up to 5 K for **8–10** with a sweep rate of 12 Oe s^{-1} (Fig. 4b, S51 and S52†). These phenomena confirm the presence of a ground state QTM process at low temperature.

Magneto-structural correlations

The effects on the anisotropic barriers of the Dy(III) complexes by substituting terminal ligands with varying electron-withdrawing substituents have been reported previously.[45] As we sequentially modify the axial pyrazolate ligands and equatorial
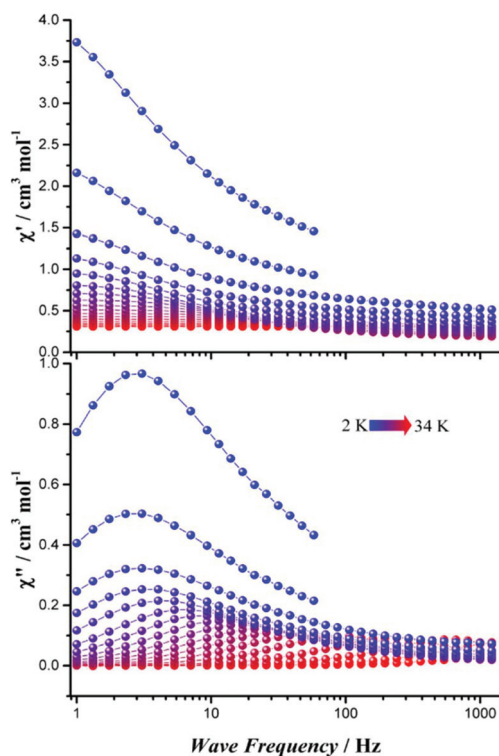

Fig. 3 Frequency-dependent in-phase (upper) and out-of-phase (lower) ac susceptibility of **8** in zero static field.

Table 1 Experimental energy barriers (U_{eff}), and key magnetic fit parameters for complexes **1–10**

Complex	U_{eff}/K	τ_0/s	C/s^{-1} K^{-n}	n/s	τ_{QTM}/s
1	—	—	0.045(2)	5.55(3)	—
2	205(2)	$5.45(3) \times 10^{-10}$	8.0(1)	2.31(3)	0.0012(2)
3	313(4)	$8.96(3) \times 10^{-11}$	2.40(4)	2.30(3)	0.0026(4)
4	360(3)	$2.70(1) \times 10^{-11}$	0.25(3)	2.90(8)	0.014(3)
5	270(8)	$1.50(2) \times 10^{-9}$	0.15(1)	3.02(5)	0.15(1)
6	470(5)	$2.00(5) \times 10^{-10}$	0.011(2)	2.83(4)	—
7	380(5)	$1.87(4) \times 10^{-11}$	0.62(1)	2.02(2)	0.0033(4)
8	521(8)	$9.05(5) \times 10^{-12}$	0.021(6)	3.01(4)	0.12(5)
9	470(6)	$8.50(3) \times 10^{-12}$	$3.5(2) \times 10^{-4}$	4.13(5)	4.55(4)
10	444(4)	$8.20(4) \times 10^{-12}$	0.0049(5)	3.77(3)	0.55(4)

4370 | *Inorg. Chem. Front.*, 2020, **7**, 4367–4376

This journal is © the Partner Organisations 2020

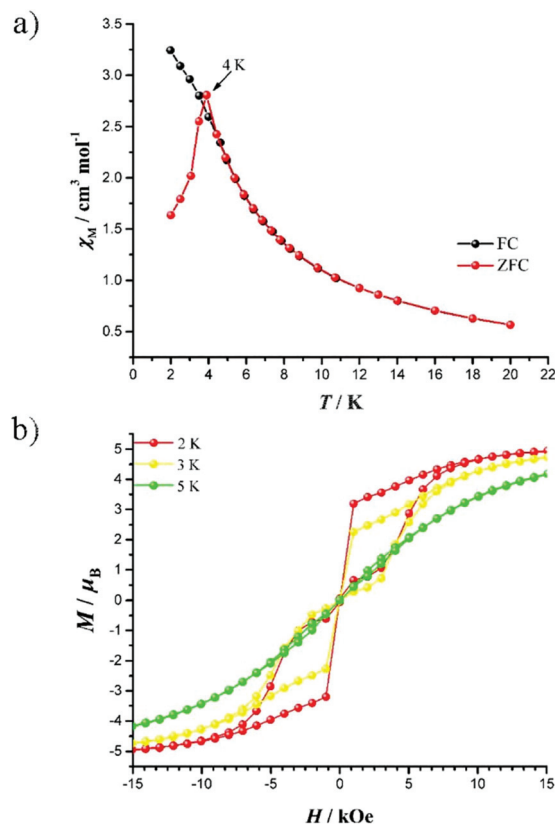**Fig. 4** (a) FC (black) and ZFC (red) magnetization plots for **8**. (b) Magnetic hysteresis loops for **8** between 2 K and 5 K with a field sweeping rate of 12 Oe s^{-1}.

Fig. 5 The zero field τ^{-1} *vs.* T plot for **1–6**. Solid lines are the best fits using equations described in the text.

Fig. 6 The zero field τ^{-1} *vs.* T plot for **7–10**. Solid lines are the best fits using equations described in the text.

solvents, while keeping the DPB geometry for the central Dy(III) ions, a potential magneto-structural correlation may be obtained for this series of complexes.

Complex **1** relaxes fast with a questionable "barrier". By comparing **1** with **2–6**, we found that as the Dy–cen(N–N) distance increases by adding electron-withdrawing substituents (Tables S1–S6†), the U_{eff} decreases. The increased bond distance between the terminal ligand and the Dy(III) centres indicates a weaker ligand field acting on the Dy(III) ions. For complexes **2–5**, in which the substituents are composed of alkyls, the Dy–cen(N–N) distances and the Cl–Dy–cen(N–N) angles are similar, indicating less electron-pushing effect (Fig. 5). Among this mono-pyrazolate series, complex **4** gives the highest effective energy barrier of 360(3) K (Table 1), which is probably due to the shorter Dy–cen(N–N) distance and the straighter Cl–Dy–cen(N–N) angle.

Similar to **1**, **7** has a lower U_{eff} value than other three complexes in the second series of complexes due to the introduction of an electron-withdrawing trifluoromethyl group. Complexes **8–10** have identical axial ligands to each other but different equatorial ligands. Within these three complexes, U_{eff} decreases from **8** to **10**, as the average Dy–cen(N–N) distance for the component in the crystal structure increases (Fig. 6).
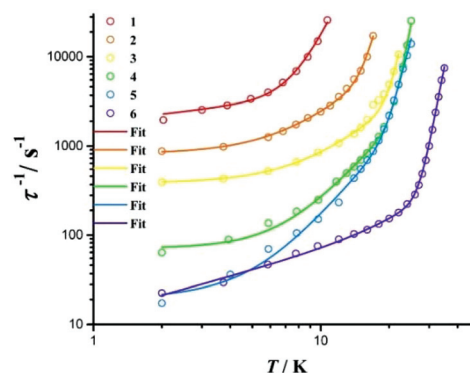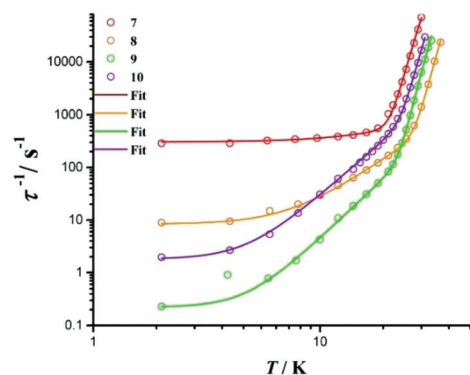
For the Raman process, all samples other than **1** show a $\tau^{-1} = CT^n$ (eqn (2)) trend with n from 2.02(2) to 4.13(5), which is reasonable for mononuclear lanthanide SMMs ($n = 2$–9). In many high-performant SMMs, n could be smaller in the presence of optical phonons (usually $n = 2$–5).[8,9,22,25,28] Combined with our previously reported pentagonal-bipyramidal complexes, they fall into two classes: one containing five THF equatorial ligands, and the other containing five py/NS equatorial ligands. Interestingly, the first class in our system possesses a lower n value (2.02–3.02 for complexes **2–8**) than that of [DyL^{1}L^2(THF)$_5$][BPh$_4$] (L^1/L$^2 = $ −OCMe$_3$, −OSiMe$_3$, −OPh, Cl$^-$ or Br$^-$) (3.7–4.7),[20,22] approaching phonon-bottleneck. Such a significant reduction indicates that our initial goal of using pyrazolate ligands to form the axial coordination is achieved successfully. For the second class, the n values of 3.77–4.13 for complexes **9** and **10** are comparable to 3.6–4.2 for [Dy(L)$_2$(py)$_5$][BPh$_4$] (HL = (S)-(−)-1-phenylethanol, *tert*-butanol, trimethylsilanol or phenol);[8,22,28] thus maybe such an idea cannot fulfil all the situations.

Interestingly, complex **8** coordinated with THF molecules possesses higher blocking temperature (T_B) with the highest ZFC peak of 4 K but hysteresis temperature open up to 5 K, which is similar to **9** and **10**. This is different from the formal

This journal is © the Partner Organisations 2020

Inorg. Chem. Front., 2020, **7**, 4367–4376 | **4371**

PB-type Dy(III) SMMs, where the py ligand can enhance the inter-/intra-molecular π–π interactions,[8,28] causing complexes coordinated with py to possess obviously higher hysteresis temperature than ones coordinated with THF. This is probably because bis-bidentate-chelating Dy(III) ions are stiff enough to ignore the interactions with the equatorial ligands, further confirming our initial motivation of using such types of bidentate pyrazolate-type ligands. Besides, due to the small steric hindrance of thiazole, the geometry configuration of complex **10** is deviated more from the ideal PB geometry, giving lower hysteresis temperature.

Electronic structure calculations

To gain insight into the magnetic properties of **1–10** on a microscopic scale, we performed *ab initio* calculations at the SA-CASSCF/RASSI level[46,47] (see the ESI† for details). According to the crystal structures, these complexes can be divided into two classes, namely **1–6** and **7–10**. The total magnetic energy splitting of **1–6** span an energy space below 620 K. The main magnetic anisotropy axes for **1–6** are all pointing to the centroid of the pyrazolate ligand through the Dy^{III} ion and collinear with the pseudo-C_5 axis. However, the energy of low-lying Kramer doublets (KDs) and possible transition pathways are largely different from each other. For **1**, the KD possesses a strongly mixed doublet with a wavefunction containing significant contributions from excited states, namely a mixture of states with $10\%|\pm15/2\rangle + 12\%|\pm11/2\rangle + 18\%|\pm9/2\rangle + 18\%|\pm7/2\rangle + 15\%|\pm5/2\rangle + 10\%|\pm3/2\rangle$, which lead to a strong QTM effect. For **2–5**, the ground doublet has a wavefunction largely based on $m_J = |\pm15/2\rangle$ (though some of them mixed with part of $|\pm13/2\rangle$ states), suggesting a possible relaxation pathway to higher KDs. For **2**, the ground KD possesses a nearly perfect axial g-tensor ($g_x = g_y = 0$ and $g_z = 19.87$) with $89\%|\pm15/2\rangle + 10\%|\pm13/2\rangle$, while the first excited KDs are constructed by $19\%|\pm13/2\rangle + 13\%|\pm5/2\rangle + 39\%|\pm3/2\rangle + 19\%|\pm1/2\rangle$ and second excited ones with $36\%|\pm13/2\rangle + 42\%|\pm1/2\rangle$. In this case, QTM with a relatively large transition probability of 3.8 and $4.8\mu_B{}^2$ between the first and second excited KDs, respectively, can be predicted. The situations for complexes **3–5** are quite similar but slightly different from those for **2**. The ground KDs show axial-type g-tensors with most contributions from the $|\pm15/2\rangle$ state, while the first excited KDs are constructed by the majority of $|\pm13/2\rangle$ states, which leads to magnetic relaxation to higher KDs. However, other higher-lying doublets are strong admixtures of the m_J functions. The most possible pathways for magnetic relaxation localize in the range of 267–340 K, 310–376 K and 258–294 K, for **3**, **4** and **5**, respectively (Fig. S58, S60 and S62†). For **6**, the axiality type can be kept up to the second KDs, leading to the best SMM behaviour observed among **1–6**. The three low-lying KDs (Table S19†) follow the order of $|\pm15/2\rangle$, $|\pm13/2\rangle$ and $|\pm11/2\rangle$, with relative energies of 0, 293 and 441 K, respectively. The subsequent excited states are highly mixed and bunched over 480 to 619 K. Using the average matrix elements of magnetic moment between the electronic states as a proxy for transition propensity, we predict the most efficient magnetic relaxation pathway to

occur *via* the highly bunched set of states with 480–491 K, as also consistent with experimentally observed U_{eff} (*ca.* 470 K).

The main magnetic anisotropy axis for **7–10** is nearly collinear with the pseudo-C_5 axis lying along the axial cen(N–N)–Dy–cen(N–N) orientation (Fig. 7b, S65, S67 and S69†). For **7**, the ground KDs are highly anisotropic with $94\%|\pm15/2\rangle$ and $g_z = 19.79$. However, due to the relatively weak coordination from the tfpz ligand, the first excited state meets with a strong mixed state with $10\%|\pm13/2\rangle + 15\%|\pm9/2\rangle + 27\%|\pm7/2\rangle + 34\%|\pm5/2\rangle$, and the magnetic axis of the g-value is perpendicular to the pseudo five-fold axis over this KD. Therefore, we would expect Orbach relaxation to proceed *via* the first and/or third excited states (319–378 K). For **8**, the ground KDs are similar to those of **7** with $96\%|\pm15/2\rangle$ and $g_z = 19.82$, but the contribution to the first KDs from $|\pm13/2\rangle$ is largely enhanced, which keeps the principal axis of the g-value parallel to the ground ones. As shown in Fig. 7a, the relaxation can step to the third excited KDs. In this case, the predicted barrier is *ca.* 503–558 K, higher than that of **7**. For **9** and **10**, the possible relaxation pathway is close to that of **8**, but the replacement of equatorial ligands leads to lowered corresponding energy levels. The predicted energy relaxation pathway is through second to fourth excited KDs (414–483 K) for **9** and (369–461 K) for **10**.
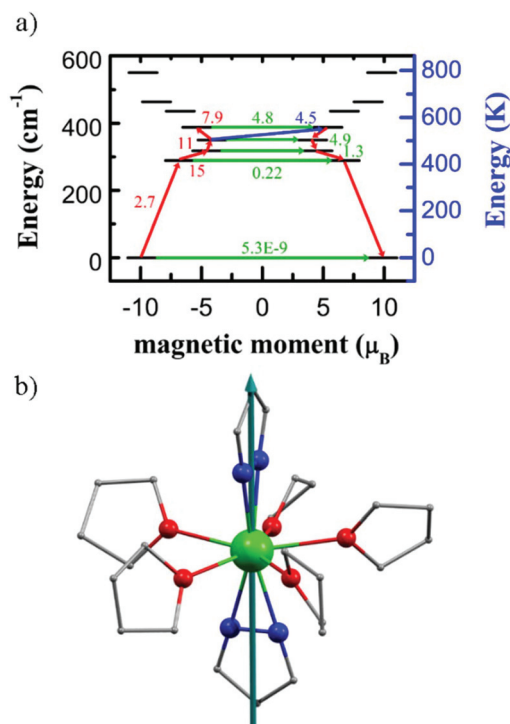

Fig. 7 (a) *Ab initio* calculated electronic states of the $J = 15/2$ manifold of the $^6H_{15/2}$ term of Dy^{III} in **8**. Arrows depict the relaxation pathway for direct vertical transitions to the first-neighbor multiplet (red), QTM (green) and Orbach/Raman relaxation (blue), while the number of the corresponding colour represents the probability of transition. (b) The principal magnetic axis of the ground Kramer's doublet of **8**. Colour codes: Dy, bright green; N, blue; O, red; C, grey.

4372 | *Inorg. Chem. Front.*, 2020, **7**, 4367–4376

This journal is © the Partner Organisations 2020

Compared to $[Dy(O^tBu)_2(py)_5][BPh_4]$ **11**, **8** (as the representative of best SMMs here) shows reduced U_{eff}. We preclude that this is its reduced axiality of the bidentate-chelating coordination mode to the Dy(III) ion, which essentially breaks the C_5 symmetry. In a microscopic view, we can find that **11** possesses much purer excited KDs than **8**. Meanwhile, since $^tBuO^-$ anions offer stronger electronegativity than pyrazolate ligands, the magnetic energy splitting is largely different (791 K for **8** vs. 1755 K for **11**).

Conclusions

In summary, a new family of air-stable dysprosium(III) SMMs with DPB geometry and different substituent pyrazolate ligands and solvent molecules are studied. Modification of the axial ligand notably suggests that the magnetic anisotropy is markedly reduced by employing electron-withdrawing substituent groups. Compared to the formal PB geometry, DPB Dy(III) SMMs are inferior to the former due to the weaker ligand field and broken axial symmetry. However, the alleviative equatorial ligand effect indicates the success of bi-dentate-chelating pyrazolate ligands, which effectively reduces the vibration from the central metal ions and peripheral ligands. Further balance between the axiality and the rigidity of the molecule is essentially critical to design high-performance Dy(III) SMMs.

Experimental section

Materials

All manipulations were performed under an atmosphere of purified argon in a glovebox or using standard Schlenk techniques. Anhydrous DyCl$_3$ salts were prepared according to literature procedures.[48] NaH, NaBPh$_4$, 3-(trifluoromethyl)pyrazole, 3-methylpyrazole, 3-isopropyl-1H-pyrazole, pyrazole, 3,5-dimethylpyrazole, and 3,5-diisopropylpyrazole were purchased commercially and used as received without further purification. THF, pyridine, thiazole and hexane were dehydrated and deoxygenated using a solvent purification system prior to use.

Synthesis

Preparation of 1. To a solution of tfpzH (68 mg, 0.5 mmol) in THF (4 mL), NaH (60% dispersion in mineral oil, 20 mg, 0.5 mmol) was slowly added under stirring. Upon complete addition, the reaction mixture was stirred for 30 min. Subsequently a suspension of anhydrous DyCl$_3$ (134.5 mg, 0.5 mmol) and NaBPh$_4$ (171.1 mg, 0.5 mmol) in about 4 mL of THF was slowly added. Then the mixture was heated to 75 °C and stirred for 12 hours. After filtration through Celite and evaporation, pale yellow crystals were isolated by layering saturated THF solution of **1** with hexane at −35 °C. Yield: 350 mg (64% based on Dy). Elemental analysis found (calcd)% for C$_{52}$H$_{70}$BClDyF$_3$N$_2$O$_6$: C, 57.46 (57.52); H, 6.37 (6.45); N, 2.57 (2.58).

Preparation of 2. Following an analogous procedure to prepare **1**, MepzH (41 mg, 0.5 mmol) is used instead of tfpzH to give **2** as colourless crystals. Yield: 287 mg (62% based on Dy). Elemental analysis found (calcd)% for C$_{48}$H$_{65}$BClDyN$_2$O$_5$: C, 59.98 (60.20); H, 6.57 (6.58); N, 2.89 (2.93).

Preparation of 3. Following an analogous procedure to prepare **1**, IprpzH (55 mg, 0.5 mmol) is used instead of tfpzH to give **3** as colourless crystals. Yield: 346 mg (66% based on Dy). Elemental analysis found (calcd)% for C$_{54}$H$_{69}$BClDyN$_2$O$_6$: C, 61.78 (61.66); H, 6.57 (6.57); N, 2.63 (2.66).

Preparation of 4. Following an analogous procedure to prepare **1**, Me$_2$pzH (48 mg, 0.5 mmol) is used instead of tfpzH to give **4** as pale yellow crystals. Yield: 308 mg (58% based on Dy). Elemental analysis found (calcd)% for C$_{53}$H$_{77}$BClDyN$_2$O$_7$: C, 59.73 (59.83); H, 7.26 (7.24); N, 2.60 (2.63).

Preparation of 5. Following an analogous procedure to prepare **1**, Ipr$_2$pzH (76 mg, 0.5 mmol) is used instead of tfpzH to give **5** as colourless crystals. Yield: 391 mg (70% based on Dy). Elemental analysis found (calcd)% for C$_{57}$H$_{85}$BClDyN$_2$O$_7$: C, 61.33 (61.23); H, 7.44 (7.43); N, 2.49 (2.51).

Preparation of 6. Following an analogous procedure to prepare **1**, pzH (34 mg, 0.5 mmol) is used instead of tfpzH to give **6** as colourless crystals. Yield: 278 mg (54% based on Dy). Elemental analysis found (calcd)% for C$_{51}$H$_{73}$BClDyN$_2$O$_7$: C, 59.55 (59.43); H, 6.57 (6.60); N, 2.69 (2.72).

Preparation of 7. Following an analogous procedure to prepare **1**, tfpzH (136 mg, 1 mmol) is used to give **7** as colourless crystals. Yield: 400 mg (72% based on Dy). Elemental analysis found (calcd)% for C$_{52}$H$_{64}$BDyF$_6$N$_4$O$_5$: C, 56.08 (56.10); H, 5.65 (5.75); N, 5.05 (5.03).

Preparation of 8. Following an analogous procedure to prepare **1**, pzH (68 mg, 1 mmol) is used instead of tfpzH to give **8** as colourless crystals. Yield: 233 mg (48% based on Dy). Elemental analysis found (calcd)% for C$_{50}$H$_{66}$BDyN$_4$O$_5$: C, 60.59 (61.45); H, 6.71 (6.76); N, 5.65 (5.74).

Preparation of 9. Following an analogous procedure to prepare **8**, the powder was dissolved in py and layered with hexane. After a few days, pale yellow crystals of **9** were obtained. Yield: 249 mg (44% based on Dy). Elemental analysis found (calcd)% for C$_{62}$H$_{58}$BDyN$_{11}$: C, 65.59 (65.81); H, 5.84 (5.13); N, 13.57 (13.62).

Preparation of 10. Following an analogous procedure to prepare **8**, the powder was dissolved in NS and evaporated slowly at room temperature. After a few days, yellow crystals were obtained. Yield: 198 mg (38% based on Dy). Elemental analysis found (calcd)% for C$_{45}$H$_{41}$BDyN$_9$S$_5$: C, 52.11 (51.85); H, 3.84 (3.94); N, 11.88 (12.10).

Air stability. All the crystals kept the original unit cells after being exposed to air for two weeks.

X-ray crystallography data

All data were recorded on a Bruker SMART CCD diffractometer with MoKα radiation (λ = 0.71073 Å). The structures were solved by direct methods and refined on F^2 using SHELXTL. CCDC 1991398 (**1**), 1991399 (**2**), 1991400 (**3**), 1991401 (**4**), 1991402 (**5**), 1991403 (**6**), 1991404 (**7**), 1991405 (**8**), 1991406 (**9**)

This journal is © the Partner Organisations 2020

Inorg. Chem. Front., 2020, **7**, 4367–4376 | **4373**

and 1991407 (**10**)† contain the supplementary crystallographic data for this paper.

Magnetic properties

Magnetic susceptibility measurements were carried out with a Quantum Design MPMS-XL7 SQUID. Freshly prepared crystalline samples were embedded in eicosane to avoid any field induced crystal reorientation. Diamagnetic corrections have been applied for the eicosane and for the molecule, the latter being calculated from the Pascal constants.

Computational method

Ab initio calculations at the SA-CASSCF/RASSI level were performed on program MOLCAS 8.0 [49] and the structure was originally taken from the X-ray structure. The basis sets were chosen from the ANO-RCC library[50] as have been used in many works.[51–53] The Dy atom was treated with VTZP quality, and then the related B, C and O atoms with VDZP quality and others with VDZ quality. The state-averaged CASSCF orbitals of the sextets, quartets and doublets were optimized with 21, 224 and 490 states, respectively, with the RASSCF module. 21, 128 and 130 sextets, quartets and doublets chosen to construct and diagonalize in spin–orbit (SO) coupling Hamiltonian with the RASSI[54] module. These computed SO states were written in the SINGLE_ANISO[55–58] program to compute the g-tensors, crystal field parameters and magnetic energy levels for the doublets of the ground $J = 15/2$ multiple of the $^6H_{15/2}$ term for Dy(III). The two electron integrals were Cholesky decomposed with a threshold of 1×10^{-8} to account for the accuracy.[59]

Conflicts of interest

The authors declare no conflict of interest.

Acknowledgements

Notes and references

1 R. Sessoli, D. Gatteschi, A. Caneschi and M. A. Novak, Magnetic Bistability in a Metal-Ion Cluster, *Nature*, 1993, **365**, 141–143.

2 L. Bogani and W. Wernsdorfer, Molecular Spintronics Using Single-Molecule Magnets, *Nat. Mater.*, 2008, **7**, 179–186.

3 F. Troiani and M. Affronte, Molecular Spins for Quantum Information Technologies, *Chem. Soc. Rev.*, 2011, **40**, 3119–3129.

4 M. Shiddiq, D. Komijani, Y. Duan, A. Gaita-AriÇo, E. Coronado and S. Hill, Enhancing Coherence in Molecular Spin Qubits via Atomic Clock transitions, *Nature*, 2016, **531**, 348–351.

5 M. Mannini, F. Pineider, P. Sainctavit, C. Danieli, E. Otero, C. Sciancalepore, A. M. Talarico, M.-A. Arrio, A. Cornia, D. Gatteschi and R. Sessoli, Magnetic Memory of a Single-Molecule Quantum Magnet Wired to a Gold Surface, *Nat. Mater.*, 2009, **8**, 194–197.

6 M. Ganzhorn, S. Klyatskaya, M. Ruben and W. Wernsdorfer, Strong Spin–Phonon Coupling Between a Single-Molecule Magnet and a Carbon Nanotube Nanoelectromechanical System, *Nat. Nanotechnol.*, 2013, **8**, 165–169.

7 S. Thiele, F. Balestro, R. Ballou, S. Klyatskaya, M. Ruben and W. Wernsdorfer, Electrically Driven Nuclear Spin Resonance in Single-Molecule Magnets, *Science*, 2014, **344**, 1135–1138.

8 K.-X. Yu, J. G. C. Kragskow, Y.-S. Ding, Y.-Q. Zhai, D. Reta, N. F. Chilton and Y.-Z. Zheng, Enhancing Magnetic Hysteresis in Single-Molecule Magnets by Ligand Functionalization, *Chem*, 2020, **6**, 1777–1793.

9 F.-S. Guo, B. M. Day, Y.-C. Chen, M.-L. Tong, A. Mansikkamäki and R. A. Layfield, Magnetic Hysteresis up to 80 Kelvin in a Dysprosium Metallocene Single-Molecule Magnet, *Science*, 2018, **362**, 1400–1403.

10 L. Ungur and L. F. Chibotaru, Strategies toward High-Temperature Lanthanide-Based Single-Molecule Magnets, *Inorg. Chem.*, 2016, **55**, 10043–10056.

11 F.-S. Guo and R. A. Layfield, Cyclopentadienyl Ligands in Lanthanide Single-Molecule Magnets: One Ring To Rule Them All?, *Acc. Chem. Res.*, 2018, **51**, 1880–1889.

12 A. K. Bar, P. Kalita, M. K. Singh, G. Rajaraman and V. Chandrasekhar, Low-Coordinate Mononuclear Lanthanide Complexes as Molecular Nanomagnets, *Coord. Chem. Rev.*, 2018, **367**, 163–216.

13 M. Feng and M.-L. Tong, Single Ion Magnets from 3d to 5f: Developments and Strategies, *Chem. – Eur. J.*, 2018, **24**, 7574–7594.

14 M. Xémard, S. Zimmer, M. Cordier, V. Goudy, L. Ricard, C. Clavaguéra and G. Nocton, Lanthanidocenes: Synthesis, Structure, and Bonding of Linear Sandwich Complexes of Lanthanides, *J. Am. Chem. Soc.*, 2018, **140**, 14433–14439.

15 J. D. Rinehart and J. R. Long, Exploiting Single-Ion Anisotropy in the Design of f-Element Single-Molecule Magnets, *Chem. Sci.*, 2011, **2**, 2078–2085.

16 L. Sorace, C. Benelli and D. Gatteschi, Lanthanides in Molecular Magnetism: Old Tools in a New Field, *Chem. Soc. Rev.*, 2011, **40**, 3092–3104.

4374 | *Inorg. Chem. Front.*, 2020, **7**, 4367–4376

This journal is © the Partner Organisations 2020

17 D. N. Woodruff, R. E. P. Winpenny and R. A. Layfield, Lanthanide Single-Molecule Magnets, *Chem. Rev.*, 2013, **113**, 5110–5148.

18 P. Zhang, Y.-N. Guo and J. Tang, Recent Advances in Dysprosium-Based Single Molecule Magnets: Structural Overview and Synthetic Strategies, *Coord. Chem. Rev.*, 2013, **257**, 1728–1763.

19 S. T. Liddle and J. van Slageren, Improving f-Element Single Molecule Magnets, *Chem. Soc. Rev.*, 2015, **44**, 6655–6669.

20 Y.-S. Ding, K.-X. Yu, D. Reta, F. Ortu, R. E. P. Winpenny, Y.-Z. Zheng and N. F. Chilton, Field- and Temperature-Dependent Quantum Tunnelling of the Magnetisation in a Large Barrier Single-Molecule Magnet, *Nat. Commun.*, 2018, **9**, 3134.

21 Y. Ma, Y.-Q. Zhai, Y.-S. Ding, T. Han and Y.-Z. Zheng, Understanding a Pentagonal-Bipyramidal Holmium(III) Complex with a Record Energy Barrier for Magnetisation Reversal, *Chem. Commun.*, 2020, **56**, 3979–3982.

22 Y.-S. Ding, T. Han, Y.-Q. Zhai, D. Reta, N. F. Chilton, R. E. P. Winpenny and Y.-Z. Zheng, A Study of Magnetic Relaxation in Dysprosium(III) Single-Molecule Magnets, *Chem. – Eur. J.*, 2020, **26**, 5893–5902.

23 Y.-S. Meng, Y.-Q. Zhang, Z.-M. Wang, B.-W. Wang and S. Gao, Weak Ligand-Field Effect from Ancillary Ligands on Enhancing Single-Ion Magnet Performance, *Chem. – Eur. J.*, 2016, **22**, 12724–12731.

24 F.-S. Guo, B. M. Day, Y.-C. Chen, M.-L. Tong, A. Mansikkamäki and R. A. Layfield, A Dysprosium Metallocene Single-Molecule Magnet Functioning at the Axial Limit, *Angew. Chem., Int. Ed.*, 2017, **56**, 11445–11449.

25 C. A. P. Goodwin, F. Ortu, D. Reta, N. F. Chilton and D. P. Mills, Molecular Magnetic Hysteresis at 60 Kelvin in Dysprosocenium, *Nature*, 2017, **548**, 439–442.

26 K. R. McClain, C. A. Gould, K. Chakarawet, S. J. Teat, T. J. Groshens, J. R. Long and B. G. Harvey, High-Temperature Magnetic Blocking and Magneto-Structural Correlations in a Series of Dysprosium(III) Metallocenium Single-Molecule Magnet, *Chem. Sci.*, 2018, **9**, 8492–8503.

27 P. Evans, D. Reta, G. F. S. Whitehead, N. F. Chilton and D. P. Mills, Bis-Monophospholyl Dysprosium Cation Showing Magnetic Hysteresis at 48 K, *J. Am. Chem. Soc.*, 2019, **141**, 19935–19940.

28 Y.-S. Ding, N. F. Chilton, R. E. P. Winpenny and Y.-Z. Zheng, On Approaching the Limit of Molecular Magnetic Anisotropy: A Near-Perfect Pentagonal Bipyramidal Dysprosium(III) Single-Molecule Magnet, *Angew. Chem., Int. Ed.*, 2016, **55**, 16071–16074.

29 Y.-C. Chen, J.-L. Liu, Y. Lan, Z.-Q. Zhong, A. Mansikkamaki, L. Ungur, Q.-W. Li, J.-H. Jia, L. F. Chibotaru, J.-B. Han, W. Wernsdorfer, X.-M. Chen and M.-L. Tong, Dynamic Magnetic and Optical Insight into a High Performance Pentagonal Bipyramidal DyIII Single-Ion Magnet, *Chem. – Eur. J.*, 2017, **23**, 5708–5715.

30 Y.-C. Chen, J.-L. Liu, L. Ungur, J. Liu, Q.-W. Li, L.-F. Wang, Z.-P. Ni, L. F. Chibotaru, X.-M. Chen and M.-L. Tong, Symmetry-Supported Magnetic Blocking at 20 K in Pentagonal Bipyramidal Dy(III) Single-Ion Magnets, *J. Am. Chem. Soc.*, 2016, **138**, 2829–2837.

31 A. B. Canaj, M. K. Singh, C. Wilson, G. Rajaraman and M. Murrie, Chemical and *in Silico* Tuning of the Magnetisation Reversal Barrier in Pentagonal Bipyramidal Dy(III) Single-Ion Magnets, *Chem. Commun.*, 2018, **54**, 8273–8276.

32 S. K. Gupta, T. Rajeshkumar, G. Rajaraman and R. Murugavel, An Air-Stable Dy(III) Single-Ion Magnet with High Anisotropy Barrier and Blocking Temperature, *Chem. Sci.*, 2016, **7**, 5181–5191.

33 S.-S. Liu, J. W. Ziller, Y.-Q. Zhang, B.-W. Wang, W. J. Evans and S. Gao, A Half-Sandwich Organometallic Single-Ion Magnet with Hexamethylbenzene Coordinated to the Dy (III) Ion, *Chem. Commun.*, 2014, **50**, 11418–11420.

34 K. L. M. Harriman, J. J. Le Roy, L. Ungur, R. Holmberg, I. Korobkov and M. Murugesu, Cycloheptatrienyl Trianion: An Elusive Bridge in the Search of Exchange Coupled Dinuclear Organolanthanide Single-Molecule Magnets, *Chem. Sci.*, 2017, **8**, 231–240.

35 J. J. Le Roy, M. Jeletic, S. I. Gorelsky, I. Korobkov, L. Ungur, L. F. Chibotaru and M. Murugesu, An Organometallic Building Block Approach To Produce a Multidecker 4f Single-Molecule Magnet, *J. Am. Chem. Soc.*, 2013, **135**, 3502–3510.

36 L. Ungur, J. J. Le Roy, I. Korobkov and M. Murugesu, Fine-tuning the Local Symmetry to Attain Record Blocking Temperature and Magnetic Remanence in a Single-Ion Magnet, *Angew. Chem., Int. Ed.*, 2014, **53**, 4413–4417.

37 J. J. Le Roy, L. Ungur, I. Korobkov, L. F. Chibotaru and M. Murugesu, Coupling Strategies to Enhance Single-Molecule Magnet Properties of Erbium-Cyclooctatetraenyl Complexes, *J. Am. Chem. Soc.*, 2014, **136**, 8003–8010.

38 S.-D. Jiang, B.-W. Wang, H.-L. Sun, Z.-M. Wang and S. Gao, An Organometallic Single-Ion Magnet, *J. Am. Chem. Soc.*, 2011, **133**, 4730–4733.

39 K. R. Meihaus and J. R. Long, Magnetic Blocking at 10 K and a Dipolar-Mediated Avalanche in Salts of the Bis(η^8-cyclooctatetraenide) Complex $[Er(COT)_2]^-$, *J. Am. Chem. Soc.*, 2013, **135**, 17952–17957.

40 S.-M. Chen, J. Xiong, Y.-Q. Zhang, Q. Yuan, B.-W. Wang and S. Gao, A Soft Phosphorus Atom to "Harden" an Erbium(III) Single-Ion Magnet, *Chem. Sci.*, 2018, **9**, 7540–7545.

41 L. Münzfeld, C. Schoo, S. Bestgen, E. Moreno-Pineda, R. Köppe, M. Ruben and P. W. Roesky, Synthesis, Structures and Magnetic Properties of $[(\eta^9\text{-}C_9H_9)Ln(\eta^8\text{-}C_8H_8)]$ Super Sandwich Complexes, *Nat. Commun.*, 2019, **10**, 3135.

42 D. Pfeiffer, B. J. Ximba, L. M. Liable-Sands, A. L. Rheingold, M. J. Heeg, D. M. Coleman, H. B. Schlegel, T. F. Kuech and C. H. Winter, Synthesis, Structure, and Molecular Orbital Studies of Yttrium, Erbium, and Lutetium Complexes Bearing η^2-Pyrazolato Ligands:

Development of a New Class of Precursors for Doping Semiconductors, *Inorg. Chem.*, 1999, **38**, 4539–4548.

43 G. B. Deacon, P. C. Junk and A. Urbatsch, Trivalent Rare Earth Complexes of the Unsymmetrical 3-(2′-Thienyl)-5-(trifluoromethyl)pyrazolate Ligand, *Eur. J. Inorg. Chem.*, 2011, 3592–3600.

44 D. Gatteschi, R. Sessoli and J. Villain, *Molecular Nanomagnets*, Oxford University Press, 2006.

45 F. Habib, G. Brunet, V. Vieru, I. Korobkov, L. F. Chibotaru and M. Murugesu, Significant Enhancement of Energy Barriers in Dinuclear Dysprosium Single-Molecule Magnets Through Electron-Withdrawing Effects, *J. Am. Chem. Soc.*, 2013, **135**, 13242–13245.

46 P.Å. Malmqvist, B. O. Roos and B. Schimmelpfennig, The Restricted Active Space (RAS) State Interaction Approach with Spin-Orbit Coupling, *Chem. Phys. Lett.*, 2002, **357**, 230–240.

47 P.Å. Malmqvist and B. O. Roos, The CASSCF State Interaction Method, *Chem. Phys. Lett.*, 1989, **155**, 189–194.

48 J. B. Reed, B. S. Hopkins, L. F. Audrieth, W. P. Selwood, R. Ward and J. J. Dejong, Anhydrous Rare Earth Chlorides, *Inorg. Synth.*, 1939, **1**, 28–33.

49 F. Aquilante, J. Autschbach, R. K. Carlson, L. F. Chibotaru, M. G. Delcey, L. De Vico, I. F. Galván, N. Ferré, L. M. Frutos, L. Gagliardi, M. Garavelli, A. Giussani, C. E. Hoyer, G. Li Manni, H. Lischka, D. Ma, P. Å. Malmqvist, T. Müller, A. Nenov, M. Olivucci, T. B. Pedersen, D. Peng, F. Plasser, B. Pritchard, M. Reiher, I. Rivalta, I. Schapiro, J. Segarra-Martí, M. Stenrup, D. G. Truhlar, L. Ungur, A. Valentini, S. Vancoillie, V. Veryazov, V. P. Vysotskiy, O. Weingart, F. Zapata and R. Lindh, MOLACS 8: New Capabilities for Multiconfigurational Quantum Chemical Calculations Across the Periodic Table, *J. Comput. Chem.*, 2016, **37**, 506–541.

50 B. O. Roos, R. Lindh, P.-Å. Malmqvist, V. Veryazov and P.-O. Widmark, Main Group Atoms and Dimers Studied with a New Relativistic ANO Basis Set, *J. Phys. Chem. A*, 2004, **108**, 2851–2858.

51 Y.-Q. Zhai, Y.-F. Deng and Y.-Z. Zheng, Pseudotetrahedral Cobalt(II) Complexes with PNP-Ligands Showing Uniaxial Magnetic Anisotropy, *Dalton Trans.*, 2018, **47**, 8874–8878.

52 Z.-H. Li, Y.-Q. Zhai, W.-P. Chen, Y.-S. Ding and Y.-Z. Zheng, Air-Stable Hexagonal Bipyramidal Dysprosium(III) Single-Ion Magnets with Nearly Perfect D_{6h} Local Symmetry, *Chem. – Eur. J.*, 2019, **25**, 16219–16224.

53 P.-B. Jin, Y.-Q. Zhai, K.-X. Yu, R. E. P. Winpenny and Y.-Z. Zheng, Dysprosiacarboranes as Organometallic Single-Molecule Magnets, *Angew. Chem.*, 2020, **59**, 9350–9354.

54 B. O. Roos, R. Lindh, P.-Å. Malmqvist, V. Veryazov and P.-O. Widmark, New Relativistic ANO Basis Sets for Actinide Atoms, *Chem. Phys. Lett.*, 2005, **409**, 295–299.

55 P. J. Stephens, F. J. Devlin, C. F. Chabalowski and M. J. Frisch, Ab Initio Calculation of Vibrational Absorption and Circular Dichroism Spectra Using Density Functional Force Fields, *J. Phys. Chem.*, 1994, **98**, 11623–11627.

56 A. D. Becke, Density-Functional Thermochemistry., III. The Role of Exact Exchange, *J. Chem. Phys.*, 1993, **98**, 5648–5652.

57 C. T. Lee, W. T. Yang and R. G. Parr, Development of the Colle-Salvetti Correlation-Energy Formula into a Functional of the Electron Density, *Phys. Rev. B: Condens. Matter Mater. Phys.*, 1988, **37**, 785–789.

58 A. D. Becke, Density-Functional Exchange-Energy Approximation with Correct Asymptotic Behavior, *Phys. Rev. A: At., Mol., Opt. Phys.*, 1988, **38**, 3098–3100.

59 T. R. Cundari and W. J. Stevens, Effective Core Potential Methods for the Lanthanides, *J. Chem. Phys.*, 1993, **98**, 5555–5565.